

Anti-site disorder and improved functionality of Mn_2NiX ($X = \text{Al}, \text{Ga}, \text{In}, \text{Sn}$) inverse Heusler alloys

Souvik Paul,¹ Ashis Kundu,¹ Biplab Sanyal,² and Subhradip Ghosh^{1, a)}

¹⁾*Department of Physics, Indian Institute of Technology Guwahati, Guwahati, Assam 781039, India*

²⁾*Department of Physics and Astronomy, Uppsala University, Box 516, 75120 Uppsala, Sweden*

(Dated: 19 October 2018)

Recent first-principles calculations have predicted Mn_2NiX ($X = \text{Al}, \text{Ga}, \text{In}, \text{Sn}$) alloys to be magnetic shape memory alloys. Moreover, experiments on Mn_2NiGa and Mn_2NiSn suggest that the alloys deviate from the perfect inverse Heusler arrangement and that there is chemical disorder at the sublattices with tetrahedral symmetry. In this work, we investigate the effects of such chemical disorder on phase stabilities and magnetic properties using first-principles electronic structure methods. We find that except Mn_2NiAl , all other alloys show signatures of martensitic transformations in presence of anti-site disorder at the sublattices with tetrahedral symmetry. This improves the possibilities of realizing martensitic transformations at relatively low fields and the possibilities of obtaining significantly large inverse magneto-caloric effects, in comparison to perfect inverse Heusler arrangement of atoms. We analyze the origin of such improvements in functional properties by investigating electronic structures and magnetic exchange interactions.

PACS numbers: 71.23.-k 71.20.Be 75.30.Sg 75.50.Cc

I. INTRODUCTION

For last couple of decades, magnetic shape memory alloys (MSMAs) have been fascinating the researchers because these materials combine different degrees of freedom like structural, magnetic, elastic, caloric etc., in a single phase. Coupling of micro-structure with magneto-crystalline anisotropy enables increase of magnetic field-induced strain (MFIS), which makes this class of smart materials suitable for micro-mechanical automotive sensors and actuators applications. Other interesting multifunctional properties exhibited by this class of materials are conventional and inverse magneto-caloric effect¹⁻⁴, barocaloric⁵, elastocaloric⁶, giant magnetoresistance^{7,8}, exchange bias⁹, kinetic arrest¹⁰, spin-glass¹¹ and strain-glass¹². In the heart of these applications is the magnetic-field driven martensitic transformation. The magnitude and sign of the magnetization difference (ΔM) between the high temperature austenite phase and the low temperature martensite phase is a key quantity responsible for the functional properties mentioned above. For example, Zeeman energy plays a crucial role in realizing the martensitic transformation in ferromagnetic shape memory alloys. An externally applied magnetic field performs two different tasks inside MSMA. Firstly, if the direction of the applied field is different from the easy magnetic axis of the material, the field tries to rotate the magnetization direction along it against the force associated with magnetic anisotropy. Secondly, the field generates driving force across the twin boundaries between martensitic variants, the associated energy is known as Zeeman en-

ergy. Since the energy required to move martensitic domains is lower than the magnetocrystalline anisotropy energy in MSMA, the pressure created by Zeeman energy increases the volume fraction of favorably oriented martensitic variants and lowers the energy of the product phase. It has been found that a large ΔM between the two phases in the presence of moderate external magnetic field H , i.e., the Zeeman term $\Delta M.H$, drives the motions of the martensitic domains facilitating the martensitic transformation^{13,14}. On the other hand, the sign of ΔM is related to the conventional or inverse magnetocaloric effect⁴. In case of the former, a magnetic field will cause a decrease in entropy when applied isothermally and an increase in temperature when applied adiabatically. In case of the later, an increase in entropy will effect a decrease of temperature leading to “magnetic cooling”, a phenomenon which can be exploited for green technology in refrigeration. For the inverse magnetocaloric effect, the magnetization in the martensitic phase has to be lower than that in the austenite phase. Recent research on MSMAs thus, have focused on exploring materials where ΔM can be suitably tuned in order to obtain large Zeeman energy with a small field and/or a substantial inverse magneto-caloric effect.

A decade ago, Ni_2MnGa was discovered as the first promising MSMA^{15,16}. However, Ni_2MnGa in the stoichiometric composition of 2:1:1 shows only conventional magneto-caloric effect. Moreover, ΔM for the system is rather small. Other materials in the Ni_2MnX ($X = \text{Al}, \text{In}, \text{Sn}$) series do not even possess shape memory properties at their stoichiometric compositions. A lot of research has taken place since then to obtain shape memory and/or inverse magneto-caloric effect in Ni_2MnX systems by tuning the electron to atom (e/a) ratio by either changing concentration ratio of Ni, Mn and X⁴ or by doping with

^{a)} Electronic mail: subhra@iitg.ernet.in

another element^{17,18}. These approaches led to the investigations into the potentials of Mn_2NiX ($X= Al, Ga, In, Sn$) systems. The exploration in Mn_2NiX materials was initiated in 1987 by Helmholtz *et al.* with their investigation in the structural and the magnetic properties of Mn_2NiSn from Neutron diffraction data¹⁹. Their study concluded that unlike the Ni_2MnX materials which form the usual Heusler structure, Mn_2NiSn crystallizes in inverse Heusler structure. The later structure forces one of the tetrahedral Mn atoms to interchange its position with octahedral Ni atom making the two Mn atoms nearest neighbors. The next significant step was investigations into the shape memory related properties of Mn_2NiGa , conducted by Liu *et al.*²⁰. The material exhibits an excellent two-way shape memory effect where the martensitic transformation temperature ($T_M \sim 270$ K) is close to room temperature and the Curie temperature ($T_C \sim 588$ K) is quite high²⁰. The last two parameters of Mn_2NiGa are better than those of Ni_2MnGa . This study hinted at the better functional properties of this material compared to the prototype and thus, generated immense interests into investigations of the Mn_2NiX materials with the possibilities of discovering new MSMA's suitable for practical applications. It is noteworthy to mention that Mn_2NiSn also has very high Curie temperature ($T_C \sim 530$ K)²¹. X-ray diffraction experiments confirmed that Mn_2NiGa also forms an inverse Heusler structure in the austenite phase. Experimental reports on the structure and shape memory property of Mn_2NiAl and Mn_2NiIn are not yet available. However theoretical calculations on Mn_2NiX confirm that all the materials exhibit shape memory effect and prefer inverse Heusler structure²². The direct consequence for crystalizing in this structure is lower saturation magnetization due to opposite and unequal moments of nearest neighbor Mn atoms, as compared to prototype Ni_2MnGa , where all the constituent atoms couple ferromagnetically. For Mn_2NiAl and Mn_2NiGa , total magnetization reported is $\sim 1 \mu_B$ and for Mn_2NiIn and Mn_2NiSn those are $\sim 0.5 \mu_B$ ²², while Ni_2MnGa posses a high moments of $\sim 4 \mu_B$. Since the MFIS is directly proportional to the total magnetization, lowering of the later would results in a smaller MFIS in Mn_2NiGa ($\sim 4\%$), whereas largest MFIS are observed in nearly stoichiometric composition of $NiMnGa$ MSMA is about 10%^{15,16}. On the contrary, Helmholtz *et al.* observed a higher value of total magnetization, nearly $2.5 \mu_B$, in cubic austenite phase of Mn_2NiSn ¹⁹. They showed that within the inverse Heusler structure, there is significant anti-site disorder among the Ni and Mn atoms at the tetrahedral positions. Recent Neutron diffraction studies^{23,24} and first principles Density Functional Theory (DFT) calculations on Mn_2NiGa ²⁵ and Mn_2NiSn ²⁶ also confirmed the presence of anti-site disorder in these materials. DFT calculations conclusively showed that such anti-site disorder is responsible for a significantly large magnetic moment in the high temperature phase. The calculations also showed that Mn_2NiGa would exhibit inverse magneto-caloric effect²⁵.

Motivated by these discoveries, in this communication, we perform DFT calculations to investigate the magnetic properties of the four Mn_2NiX alloys which are potential MSMA's, in crystal structures relevant to the austenite and martensite phases, with and without anti-site disorder. We specifically looked at the trends in ΔM across the series. We analyze the results by computing the electronic structures and the inter-atomic exchange interactions for each of the cases. The outcome of this systematic study indicates that the Mn_2NiX alloys may have better functionalities than the prototype MSMA's, which is driven by the anti-site disorder inherent to these systems, an important feat relevant in today's technology. The paper is organized as follows: In Section II, we discuss the computational details. Section III contains the results and subsequent discussions on the magnetic properties, the electronic structure and the inter-atomic exchange interactions. Summary and importance of this work are described in the conclusions section.

II. COMPUTATIONAL DETAILS

The electronic structures of the materials concerned have been calculated using Full-potential based Spin-Polarized Relativistic Korringa-Kohn-Rostoker (SPR-KKR) Green's function method^{27,28}. The Local Spin Density Approximation (LSDA) as parameterized by Vosko-Wilk-Nusair (VWN) was used as the exchange-correlation part of the potential to solve the Kohn-Sham equation²⁹. The angular momentum cut-off to the plane wave was taken to be $\ell_{max}=3$. The Brillouin zone integrations have been carried out on a uniform $24 \times 24 \times 24$ k -mesh. The Green's function was calculated for 30 complex energy points distributed exponentially on a semicircular contour. The energy convergence criterion was set to 10^{-6} Ry for the self-consistent cycles. The Coherent Potential Approximation (CPA) was used to incorporate the effects of disorder³⁰.

The magnetic pair exchange interactions have been calculated with multiple scattering Green function formalism as implemented in SPR-KKR code²⁸. Spin fluctuation theories for metals map the complicated itinerant electron systems onto an effective Heisenberg Hamiltonian having the classical spins as

$$H_{eff} = - \sum_{\mu, \nu} \sum_{i, j} J_{ij}^{\mu\nu} \mathbf{e}_i^\mu \cdot \mathbf{e}_j^\nu \quad (1)$$

The indices μ and ν represent different sublattices, i and j denote the atomic positions and \mathbf{e}_i^μ is the unit vector along the direction of magnetic moments at site i belonging to sublattice μ . The size of the magnetic moments are included in the exchange interaction parameter $J_{ij}^{\mu\nu}$. The exchange parameters are computed from energy difference due to the small orientation of a pair of spins resulting a perturbation in spin-density which within the formulation of Lichtenstein *et al.*³¹ based on magnetic

force theorem³² takes the following form

$$J_{ij}^{\mu\nu} = \frac{1}{4\pi} \int_{-\infty}^{E_F} d\epsilon \Im \text{Tr}(\Delta_i \hat{T}_{\sigma}^{ij} \Delta_j \hat{T}_{\sigma}^{ji}) \quad (2)$$

where $\Delta_i = \hat{t}_{i\sigma}^{-1} - \hat{t}_{i\sigma}$, σ is the spin index, \hat{t} is the single site scattering matrix and \hat{T} is the scattering path operator related to the off-diagonal elements of the Green's function. Tr is the trace over the orbital indices of the scattering matrix. Positive (negative) values for $J_{ij}^{\mu\nu}$ indicate ferromagnetic (antiferromagnetic) coupling between atoms i and j .

TABLE I. Sublattice occupancies corresponding to the configurations used. The details are described in the text.

Configuration	Sublattice			
	(000)	$(\frac{1}{2}\frac{1}{2}\frac{1}{2})$	$(\frac{1}{4}\frac{1}{4}\frac{1}{4})$	$(\frac{3}{4}\frac{3}{4}\frac{3}{4})$
OC,OT	MnI	Ni	MnII	X
DC,DT	(MnI _{0.5})Ni _{0.5}	(MnI _{0.5})Ni _{0.5}	MnII	X

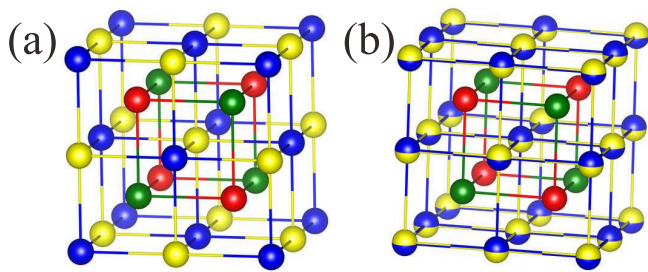


FIG. 1. (Color online) The crystal structure of Mn_2NiX in (a) **OC** and in (b) **DC** configurations. The blue, green, yellow and red spheres represent MnI, MnII, Ni and X atoms, respectively. The two-toned spheres (blue and yellow) represent sublattices with Ni-MnI alloys.

Table I shows different configurations used in this work. Space group $Fm\bar{3}m$ has been used for the cubic austenite phase and $Fmmm$ for the tetragonal martensitic phase. The configurations without anti-site disorder, i.e., ones corresponding to the perfect inverse Heusler arrangement have been referred to as **OC** (Ordered Cubic) and **OT** (Ordered Tetragonal), while the ones with anti-site disorder have been referred to as **DC** (Disordered Cubic) and **DT** (Disordered Tetragonal). In cases of **OC** and **OT**, the sublattices with octahedral symmetries are occupied by the X element and one of the Mn atoms (referred to as MnII), while the sublattices with tetrahedral symmetries are occupied by Ni and the other Mn atom (referred to as MnI). In cases of **DC** and **DT**, the tetrahedral sublattices have anti-site disorder and hence they consist of binary alloys of MnI and Ni, $\text{MnI}_x\text{Ni}_{1-x}$. The concentration x is found to vary depending upon the system and the experiment^{19,23}; hence we have considered x to be 0.5 uniformly across all systems. The reasons for

choosing $x = 0.5$ are as follows: first, the neutron diffraction results on Mn_2NiGa suggested that the occupancies of sublattices in the inverse Heusler structure in the system would be like the configuration considered here²³; for Mn_2NiSn , although the value of x suggested by the experiment was slightly different¹⁹, the results of first-principles calculations²⁶ showed that there are small differences between the magnetizations (over a sufficiently large range of volume) calculated with the system being in the configuration of Table I and that calculated using the configuration suggested by the experiment, and second, the choice of $x = 0.5$ maximizes the anti-site disorder on the tetrahedral sites. For example, $x = 0.4$ at the MnI site and $x = 0.6$ at the Ni site produces the same configuration as the one with $x = 0.6$ at the MnI site and $x = 0.4$ at the Ni site since the MnI and Ni sites are crystallographically equivalent. Moreover, $x > 0.5$ at any of the two sites produces a configuration closer to the “ordered” (**OC** or **OT**) one. Figure I shows the schematic representation of the **OC** and **DC** structures.

However, before proceeding further with the **DC** and **DT** configurations, one must make sure that

$$F_{DC} < F_{OC}, \quad F_{DT} < F_{OT}$$

Here F_{DC} , F_{OC} , F_{DT} and F_{OT} refer to the free energies in the four configurations respectively. These equations make sure that the “anti-site disordered” configurations are the thermodynamically favorable ones over the “ordered” ones, thus, making the justifications for analyzing results obtained with the “anti-site disordered” configurations any further. On top of this, one also has to make sure that the energy of the tetragonal phase in the “anti-site disordered” configuration is lower than that of the cubic phase in the same configuration, for each of these systems. Unless this occurs, further investigations into the systems exploring improved functionalities, based upon magnetizations in the austenite and in the martensite phases, would be useless.

In what follows, we compute the following quantities

$$\begin{aligned} \Delta E_{str}^{O/D} &= E_{tet}^{O/D} - E_{cub}^{O/D} \\ \Delta F_{ord}^C &= F_{OC} - F_{DC} \\ \Delta F_{ord}^T &= F_{OT} - F_{DT} \end{aligned}$$

ΔE_{str}^O and ΔE_{str}^D refer to the energies required for structural transition from the cubic to the tetragonal phase when the system is in “ordered” configuration **O** and in “anti-site disordered” configuration **D**, respectively. A negative value of $E_{str}^{O/D}$ means that the tetragonal phase is energetically lower than the cubic phase in the **O/D** configuration and that the martensitic transformation is possible. ΔF_{ord}^C and ΔF_{ord}^T are the free energies of the configuration **O** with reference to those of the configuration **D** in the cubic (C) and in the tetragonal (T) phases, respectively. The free energy expression considered here is,

$$F = E + \frac{k_B T}{N} \sum_i x_i \ln x_i + (1 - x_i) \ln (1 - x_i)$$

E is the electronic energy per atom, k_B is the Boltzmann constant, T is the temperature, N is the number of atoms, i is the sublattice index and x_i is the concentration of sublattice i . Here we have considered only the contribution of the configurational part to the entropy and neglected the effects of the lattice vibrations and electronic temperatures. At ambient conditions, the effect of the electronic temperature are negligible. The contribution from lattice vibration to the free-energy difference for alloys with different site-occupation configurations can be estimated approximately from the high-temperature expansion of the phonon free energy $\Delta F_{ph} \sim 3kT(\Delta\Theta/\Theta)^{33}$. In the simplest approximation, the Debye temperatures Θ are proportional to $\sqrt{r}B^{34}$, where r is the Wigner-Seitz radius and B is the bulk modulus. For the systems considered here, the lattice constants and hence the Wigner-Seitz radii differ only slightly between the **O** and the **D** configurations; same happens for Bulk moduli. Consequently, the contributions from vibrational part to the entropy are orders of magnitude smaller than the electronic contributions. In this paper, we have calculated the contributions from configurational entropy to the free energies only at $T = 300$ K.

In materials with chemical disorder, particularly in systems where constituents have large size differences such as Mn_2NiIn and Mn_2NiSn , there can be substantial relaxations of the local bonds. For Mn_2NiSn , the impact of such relaxations were found to be non-negligible²⁶. Since incorporation of the relaxations is not possible within the framework of the KKR-CPA method, we compute $\Delta E_{str}^{O/D}$, ΔF_{ord}^C , ΔF_{ord}^T by VASP plane wave code employing the Projector Augmented Wave approach^{35,36}. In order to mimic the chemical disorder for “anti-site disordered” configurations, we consider 64 atom supercells with MnI and Ni atoms occupying the sites with tetrahedral symmetry randomly. We also construct a 64 atom “Special Quasi-random Structure” (SQS)³⁷ which supposedly simulates the environments around an atom in a chemically disordered alloy better as the SQS is generated by matching the maximum number of correlation functions to their exact values in the real disordered alloy. The SQS structures used in this work are generated with the ‘Alloy Theory Automated Toolkit’ (ATAT) package³⁸. 50 pairs and 30 triplets having correlation functions exactly equal to those for a real disordered alloy with the same composition were chosen to construct the SQS. The total energies were calculated with both the supercell and the SQS structure. In each case, all atoms were relaxed keeping the volume fixed. A large basis was used with a plane wave cut-off of 450 eV. The exchange-correlation functional used was the same as that used in KKR calculations. Convergences of the electronic structures were assumed when changes between two consecutive steps were less than 10^{-5} eV. Atomic relaxations were carried out until all the forces were less than 10^{-3} eV/Å. A k -point mesh consisting of at least 9 k points in the irreducible part of the Brillouin Zone was considered and was sufficient for convergences of total energies and

forces.

III. RESULTS AND DISCUSSIONS

A. Structural parameters of Mn_2NiX

The experimental information on structural parameters for cubic phase are available for Mn_2NiGa ^{20,23} and Mn_2NiSn ¹⁹ only, while the information on the structural parameters in the tetragonal phase is available for Mn_2NiGa alone. In this work, we have, therefore, used the experimental lattice parameters of Mn_2NiGa in both phases and of Mn_2NiSn in the cubic phase. The lattice parameters for the other two alloys in both phases and for Mn_2NiSn in tetragonal phase were calculated by first-principles DFT. The results are tabulated in Table II.

TABLE II. The lattice parameters for Mn_2NiX systems used in this work. a_{cubic} and a_{tet} are the lattice constants in the cubic and tetragonal phases respectively, $(c/a)_{tet}$ is the global minima in the tetragonal phase.

Systems	lattice constant	lattice constant	$(c/a)_{tet}$
	$a_{cubic}(\text{Å})$	$a_{tet}(\text{Å})$	
Mn_2NiAl	5.57	3.71	1.20
Mn_2NiGa	5.90	3.92	1.21
Mn_2NiIn	5.96	3.91	1.26
Mn_2NiSn	6.10	4.06	1.20

The results obtained for **OC** and **OT** configurations using SPRKKR and VASP codes were nearly identical, with a maximum difference less than 1%. The same set of lattice parameters have been used for “ordered” and “disordered” configurations since it was found out that they hardly change from one configuration to another. It is worth mentioning that the lattice constants of Mn_2NiGa and Mn_2NiSn , in their cubic phases, calculated by DFT are 5.64 Å and 5.92 Å respectively. The DFT results differ by 3.5 – 4% compared to the experimentally obtained lattice parameters, presumably due to the LSDA functionals. We found that this discrepancy is consistent irrespective of the basis set used.

B. Stabilities of different configurations

In Table III, we show our results on $\Delta E_{str}^{O/D}$, ΔF_{ord}^C and ΔF_{ord}^T , obtained after relaxations of atomic positions in the supercell and in the SQS structure calculated by the VASP code. We note that apart from qualitative agreement on the trends, the quantitative agreement is also close between the two different supercells simulating the “anti-site disordered” configurations. We find that $\Delta E_{str}^D > 0$ for Mn_2NiAl implying that in the “anti-site disordered” configuration, the martensitic transformation does not take place. Therefore, this system in the

disordered configuration would not be suitable for the functionalities related to martensitic phase transformations and thus we exclude this system from the rest of our discussions. For the other three systems, $\Delta E_{str}^D < 0$ along with $\Delta F_{ord}^{C/T} < 0$ implying that the “anti-site disordered” configuration (**D**) is thermodynamically favorable over the ordered configuration **C** for each of these systems irrespective of the crystal structure, and that the martensitic transformation takes place in all of them with the configuration **D**.

These results, thus justify the choice of the particular disordered configuration considered in this work and further investigations into its impacts on the functional properties can be carried out.

C. Magnetic moments of Mn_2NiX

In what follows, we compute the magnetic moments, the electronic structures, the exchange interactions and the Curie temperatures for Mn_2NiGa , Mn_2NiIn and Mn_2NiSn in **OC**, **OT**, **DC** and **DT** configurations using the KKR-CPA method. Previous works^{20,22,26} have established that the ground state in all four systems considered here is ferrimagnetic. Accordingly, the starting spin configurations between two nearest neighbor Mn atoms in all four configurations considered are kept anti-parallel. In the **DC** and **DT** configurations, the MnI atoms occupying the sublattices with tetrahedral symmetry are considered to be parallel in the beginning as they are not the nearest neighbors. These starting configurations lead to the lowest energy states. The calculated total and partial magnetic moments of Mn_2NiX materials, excluding Mn_2NiAl , in all four configurations are summarized in Table IV.

The central quantity related to multi-functionalities in the present context, ΔM is defined as $\Delta M = M_{tot}^{martensite} - M_{tot}^{austenite}$, the total moment in the martensite phase with respect to that in the austenite phase for a given occupancy of the sublattices. Calculated values of ΔM are also presented in Table IV. The results show the following trends:

(i) The magnetic moments in the martensitic phase is lower than that in the austenite phase for both “ordered” and “disordered” configurations and for all three alloys under consideration, making $\Delta M < 0$.

(ii) For the “disordered” configurations, that is, both **DC** and **DT**, the magnetic moments are substantially higher than their “ordered” counterparts, i.e., **OC** and **OT** respectively. The increment is significantly greater in austenite phases than that in the martensitic phases. The total moment increases by 69%, 104% and 235% for Mn_2NiGa , Mn_2NiIn and Mn_2NiSn respectively as configuration changes from **OC** to **DC**. In the martensitic phases, the increase in moments as configuration changes from **OT** to **DT** are 27%, 22% and 342% for Mn_2NiGa , Mn_2NiIn and Mn_2NiSn respectively. This results in a huge gain in ΔM in the “anti-site disordered” configura-

tions over that in the “ordered” configurations.

The behavior of the magnetic moments across crystal structures, configurations and materials, are driven by the crystallographically inequivalent Mn atoms. The results suggest that the ferrimagnetic ground states are achieved due to the anti-parallel alignments of the MnI and MnII atoms. In the “ordered” configurations, the magnitude of the moments compensate each other substantially resulting in relatively low moments. Drastic changes are observed in cases of anti-site disorder. The substantially high moments in **DC** and **DT** configurations are driven by considerable quenching of Mn moments at the sites where they form alloys with Ni. The moments of the other Mn atom remain nearly unaltered. The Ni moments, on the other hand, increases significantly, bringing in an increase in the net moments. The changes are more dramatic in the austenites where the MnI moment changes between 37 – 54% as compared to changes between 8 – 30% in the martensites.

The significant changes in the MnI moments driven by the anti-site disorder coupled with a substantially larger changes in the total moments in the austenites lead to larger ΔM when anti-site disorder affects the sublattices with tetrahedral symmetry in the inverse Heusler structure. This is a significant result as it shows that all three Mn_2NiX alloys may exhibit inverse magneto-caloric effects and a large Zeeman energy can be achieved with relatively small magnetic field making them attractive from the point of view of shape memory applications. It may be noted that the prototype MSMA Ni_2MnGa has $\Delta M > 0$ and the magnitude of ΔM is only $0.2\mu_B$ ³⁹. Thus, Mn_2NiX alloys turn out to be MSMAs with better functional parameters even with the stoichiometric composition of 2:1:1. In the sections IIID and IIIE, we explore the origin of these magnetic properties by discussing results on electronic structures and magnetic exchange interactions.

D. Electronic structure of Mn_2NiX and dependencies on configurations

Figs. 2-4 show a comprehensive comparative presentation of the densities of states in various configurations for the three systems considered. In each figure, panels (a)-(d) show comparisons of total and partial densities of states (of magnetic components) for **OC** and **DC** configurations. Panels (e)-(h) of each figure show comparisons of same quantities for **DC** and **DT** configurations. The comparisons between **OC** and **OT** configurations for these systems had already been done²².

The densities of states of all three alloys in the **OC** configuration show certain common features: the MnI densities of states have characteristic unfilled majority bands as can be inferred by presence of substantial states in the unoccupied part, while MnII have same characteristics associated with their minority bands. This explains the reasons for getting substantial compensation of Mn

TABLE III. Compilation of $\Delta E_{ord}^{O/D}$, ΔF_{ord}^C , ΔF_{ord}^D for Mn_2NiX materials calculated for 64 atom supercell and 64 atom SQS. Calculations are done by VASP-PAW code.

Systems	64 atom supercell				64 atom SQS			
	ΔF_{ord}^C (meV/ atom)	ΔF_{ord}^T (meV/ atom)	ΔE_{str}^O (meV/ atom)	ΔE_{str}^D (meV/ atom)	ΔF_{ord}^C (meV/ atom)	ΔF_{ord}^T (meV/ atom)	ΔE_{str}^O (meV/ atom)	ΔE_{str}^D (meV/ atom)
Mn ₂ NiAl	32	9.7	-8.11	14.6	37	8.9	-8.2	19.9
Mn ₂ NiGa	10.0	3.5	-22.4	-15.8	9	3.6	-21.6	-16.8
Mn ₂ NiIn	31	11.4	-20.6	-1.5	28.6	12.1	-19.9	-3.4
Mn ₂ NiSn	30	27.7	-5.83	-3.2	32.4	37.4	-4.2	-2.2

TABLE IV. Total (M_{tot}) and partial (M_i) moments of the constituent atoms for Mn_2NiX materials in four different configurations. ΔM represents the total moment in martensite phase with respect to that in the austenite phase for a given sub-lattice occupancy (either **O** or **D**).

Systems	Config.	M_{tot} (μ_B /f.u.)	M_{MnI} (μ_B)	M_{MnII} (μ_B)	M_{Ni} (μ_B)	M_X (μ_B)	Config.	M_{tot} (μ_B /f.u.)	M_{MnI} (μ_B)	M_{MnII} (μ_B)	M_{Ni} (μ_B)	M_X (μ_B)	ΔM (μ_B)
Mn ₂ NiGa	OC	1.26	-2.27	3.17	0.35	0.01	OT	1.12	-2.27	3.05	0.33	0.01	-0.01
	DC	2.13	-1.42	3.15	0.40	0.00	DT	1.42	-2.02	3.07	0.36	0.01	-0.71
Mn ₂ NiIn	OC	1.02	-2.42	3.17	0.27	-0.00	OT	1.00	-2.30	3.02	0.28	0.00	-0.02
	DC	2.09	-1.40	3.15	0.35	-0.01	DT	1.22	-2.10	3.01	0.31	0.00	-0.86
Mn ₂ NiSn	OC	0.71	-2.74	3.33	0.11	0.01	OT	0.38	-2.84	3.19	0.04	-0.01	-0.33
	DC	2.38	-1.26	3.40	0.23	0.01	DT	1.68	-1.96	3.34	0.29	0.02	-0.70

TABLE V. The inter-atomic distances (in Å) between the magnetic atoms for Mn_2NiX systems in cubic and tetragonal phases.

Systems	Cubic			Tetragonal		
	MnI-MnII	Ni-MnI	MnII-Ni	MnI-MnII	Ni-MnI	MnII-Ni
Mn ₂ NiGa	2.56	2.95	2.56	2.58	2.77	2.58
Mn ₂ NiIn	2.58	2.98	2.58	2.61	2.76	2.61
Mn ₂ NiSn	2.64	3.05	2.64	2.66	2.87	2.66

moments leading to rather small total moments. The features in the minority bands near the Fermi level emerge due to hybridizations between MnI and Ni $3d$ states. For Mn₂NiGa and Mn₂NiIn, such hybridizations give rise to a small peak around -0.25 eV in the minority bands while for Mn₂NiSn, a prominent peak around -0.5 eV emerges. The prominent peaks in the occupied part of the minority bands such as the ones between -1 eV and -2 eV also arise from the hybridizations of same states. The majority bands for all three systems too have common characteristics; the features in the occupied parts arise due to hybridizations between Ni and MnII states.

Significant modifications to the densities of states in the **OC** configurations occur due to anti-site disorder between MnI and Ni sites. Expectedly, major changes in the electronic structure come from the MnI and the Ni densities of states. The total densities of states in the majority spin channel become rather featureless and flat in the **DC** configurations. The densities of states in the minority bands, although still retain some of the structures, but become smooth in general. For example, the peaks

near the Fermi level in the minority bands of Mn₂NiGa and Mn₂NiIn and the peaks at the Fermi level in the minority bands of Mn₂NiSn are all broadened in the **DC** configuration. MnI densities of states are affected most followed by the Ni ones. The minority spin MnI peaks (around -1.5 eV for Mn₂NiGa and Mn₂NiIn, and around -2 eV for Mn₂NiSn) broaden considerably and move closer to Fermi level (around -1.4 eV for Mn₂NiGa and Mn₂NiIn, and around -1.3 eV for Mn₂NiSn). The peaks near or at the Fermi level in the minority channels are now destroyed producing a continuously increasing densities of states near the Fermi levels. The peaks in the unoccupied parts of the majority bands of MnI atoms are severely modified: their intensities decrease considerably and they flatten out into broad plateaus extending into the occupied parts. Thus, the occupied parts in the majority bands start to get filled with states. Consequently, the magnetic moments of MnI atoms decrease in magnitudes as compared to the ones in the **OC** configurations. Densities of states in both spin channels associated with Ni too get modified with sharp peaks in **OC** configu-

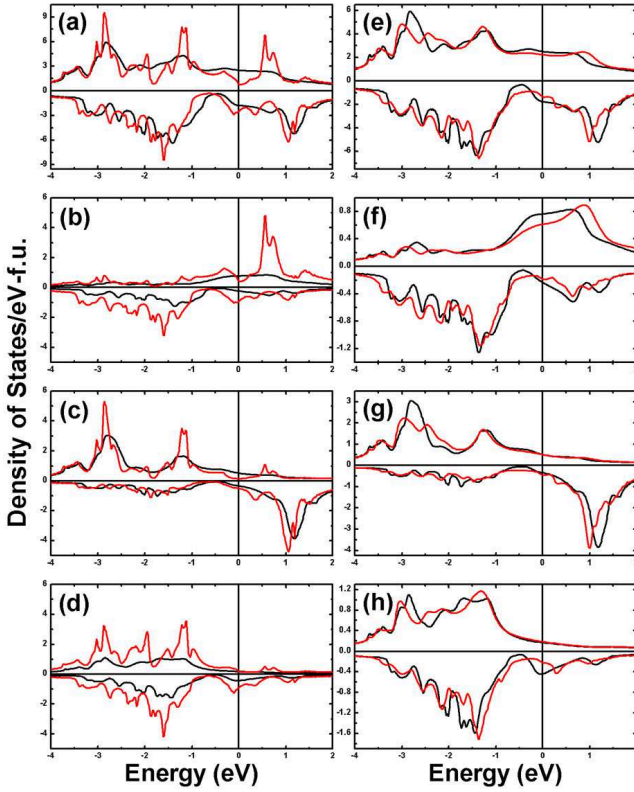


FIG. 2. (Color online) Total and partial densities of states for Mn_2NiGa . In panels (a)-(d) black curves stand for **DC** configuration and red curves stand for **OC** configuration. In panels (e)-(h), black curves denote the **DC** configuration and red curves denote the **DT** configuration. (a)-(d) and (e)-(h) panels display total, MnI, MnII and Ni densities of states, respectively.

rations getting broadened in general. The states in the minority channels start to shift towards the Fermi level, while there is hardly any shift in the states in the majority channels (comparison of panels (d) and (h) illustrate these clearly). These features explain the slight increases in the Ni moment in the **DC** configurations in comparison to the **OC** configurations of all three alloys. The anti-site disorder between MnI and Ni sites do not affect MnII densities of states substantially. The major features of the MnII densities of states in **OC** configuration do not change in **DC** configurations, the peaks only broaden explaining why the MnII moments remain almost intact in spite of anti-site disorder. To summarize, the drastic re-distribution of electronic states in both spin channels of primarily MnI atoms, brought about by the anti-site disorder between the sites of same point group symmetry, quenches the MnI moments substantially reducing the exchange splitting and thereby increasing the total magnetic moment significantly as compared to the **OC** configurations. The degree of this increment depends on the degree of changes in the MnI densities of states. The maximum changes occur in Mn_2NiSn , where, the peak at -2 eV in the MnI minority band moves substantially to-

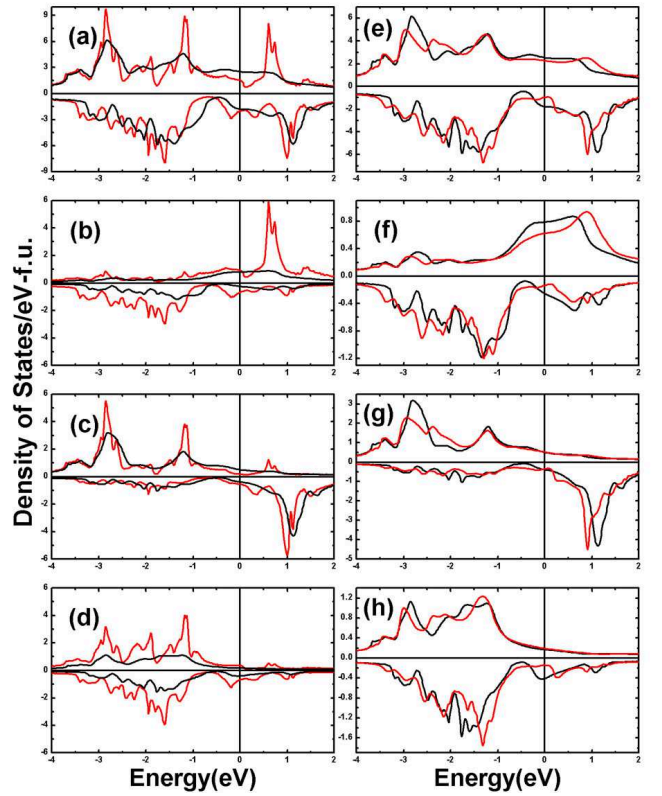


FIG. 3. (Color online) Total and partial densities of states for Mn_2NiIn . In panels (a)-(d) black curves stand for **DC** configuration and red curves stand for **OC** configuration. In panels (e)-(h), black curves stand for **DC** configuration and red curves stand for **DT** configuration. (a)-(d) and (e)-(h) panels display total, MnI, MnII and Ni densities of states, respectively.

wards the Fermi level, relocating itself at -1.25 eV as one goes from **OC** to **DC**, the other peaks too make such a move, affecting the electron distribution considerably, explaining why the changes in the moments are the largest in the series.

The reason behind obtaining a large ΔM when anti-site disorder is present, as compared to the “ordered” configurations is that the magnetic moments do not change as substantially as the systems undergo martensitic transformations. The percentage changes quoted in Section III C exemplify this. In order to understand the reasons behind this, one needs to inspect the panels (e)-(h) in FIG. 2-4 where comparisons between densities of states in the **DC** and **DT** configurations are done. The results suggest that for all three materials, the total densities of states at the Fermi level in the **DT** configurations are less than that in the **DC** configurations. This provides a clue to the stability of the martensitic phases. In fact, the densities of states are suppressed prominently in the minority bands of between -0.3 eV and the Fermi level in the **DT** configurations. In contrast, the minority densities of states in **DT** configurations for all three materials get elevated as compared to the **DC** configu-

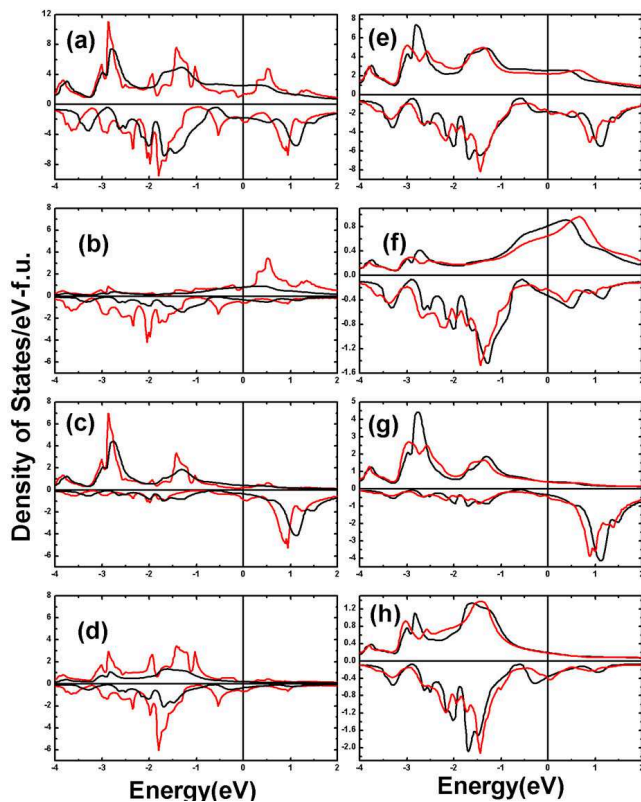


FIG. 4. (Color online) Total and partial densities of states for Mn_2NiSn . In panels (a)-(d) black curves stand for **DC** configuration and red curves stand for **OC** configuration. In panels (e)-(h), black curves stand for **DC** configuration and red curves stand for **DT** configuration. (a)-(d) and (e)-(h) panels display total, MnI, MnII and Ni densities of states, respectively.

rations between -0.3 eV and -1 eV. These undoubtedly point to the fact that electron states are transferred to the lower energies as the systems undergo martensitic transformations, explaining the stabilizations of the martensitic phases.

From the atom projected densities of states, it is clear that the hybridizations of Ni-MnI $3d$ minority electrons are responsible for such re-distributions of electronic states when the system undergoes a tetragonal deformation. Due to the tetragonal distortion, the Ni-MnI hybridizations strengthen due to the significant reductions of the Ni-MnI bond distances. Table V shows the bond distances between various Mn atoms in the austenite and in the martensitic phases. The results clearly demonstrate that only the Ni-MnI inter-atomic distances reduce by almost 6% in all the cases. On the other hand, the changes in the majority band electronic structures due to tetragonal distortions are overwhelmingly due to the MnI states. A comparison between **DC** and **DT** configurations show that states in the MnI majority bands are pushed into the unoccupied part as the systems undergo martensitic transformations. This coupled with the shifting of minority states towards lower energies produce a

larger exchange splitting of MnI resulting in an increase of the net MnI moment as compared to the austenitic phases. Thus the total moment in the martensitic phases do not change as much as they do in the austenite phases upon changes in the sublattice occupancies due to anti-site disorder in the sites with tetrahedral symmetries, resulting in a larger ΔM in the “disordered” configurations.

E. Exchange interactions and Curie temperatures of Mn_2NiX

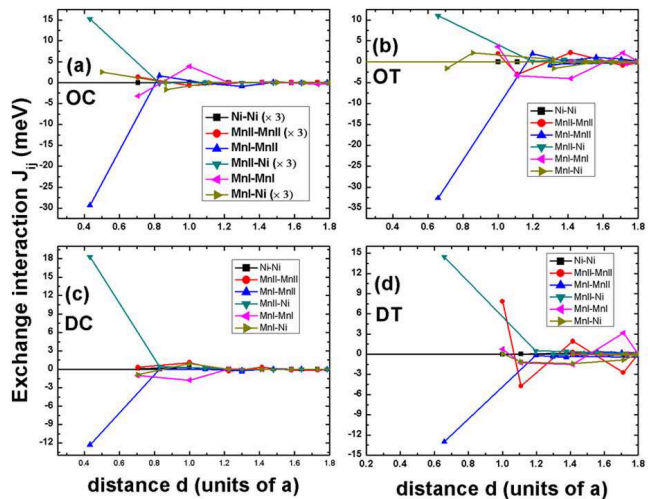


FIG. 5. (Color online) Magnetic exchange interactions (J_{ij}) as a function of inter-atomic distance d for Mn_2NiGa . Panel (a), (b), (c) and (d) represent ordered cubic (**OC**), ordered tetragonal (**OT**), disordered cubic (**DC**) and disordered tetragonal (**DT**) configurations, respectively.

In this section, we show comparative results on inter-atomic exchange interactions across structures, configurations and materials in order to understand the trends in the magnetic properties of Mn_2NiX series. In FIG. 5-7 we present results on inter-sublattice and intra-sublattice exchange interactions. The results suggest that in all three materials, the magnetic properties are governed by competitions between two interactions: Ni-MnII and MnI-MnII. The MnI-MnII interactions are anti-ferromagnetic while the Ni-MnII interactions are ferromagnetic. Comparisons of **OC** and **OT** configurations show that upon tetragonal distortions, the anti-ferromagnetic MnI-MnII interactions strengthen while the ferromagnetic Ni-MnII interactions weaken, resulting in a net loss of MnII moments and subsequent low moments in the **OT** configurations. Drastic modifications in the exchange interactions are observed due to anti-site disorder. A comparison between **OC** and **DC** configurations show that for all three alloys, the Ni-MnII interactions strengthen that is become more ferromagnetic while the MnI-MnII interactions weaken substantially. The weakening of the most

prominent anti-ferromagnetic interaction and strengthening of the most prominent ferromagnetic interaction in presence of anti-site disorder, strengthen the ferromagnetic interactions in the systems resulting in the enhancement of the overall magnetic moments when anti-site disorder is present. However, comparative assessments of **DC** and **DT** configurations show that upon tetragonal distortions, the ferromagnetic Ni-MnII interactions weaken and the anti-ferromagnetic MnI-MnII interactions strengthen. The weakening of the former being substantial, the anti-ferromagnetic interactions in the **DT** configurations are more significant than those in the **DC** configurations, resulting in a lower total moment in the former configurations in comparison to the later ones.

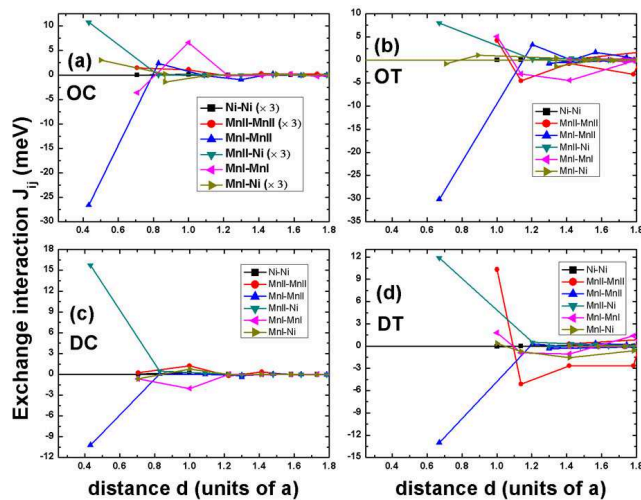


FIG. 6. (Color online) Magnetic exchange interactions (J_{ij}) as a function of inter-atomic distance d for Mn_2NiIn . Panel (a), (b), (c) and (d) represent ordered cubic (**OC**), ordered tetragonal (**OT**), disordered cubic (**DC**) and disordered tetragonal (**DT**) configurations, respectively.

The intra-sublattice exchange interactions are much weaker than the inter-sublattice ones and thus do not contribute enough to understand the trends in the magnetic properties. However, unlike the inter-sublattice ones, no common trend across the materials is observed in some of these interactions. The Ni-Ni interactions are the weakest and are weakly ferromagnetic for all materials and for all configurations. The MnI-MnI interactions are oscillatory in the **OC** configurations and become slightly anti-ferromagnetic in the **DC** configurations. In the **DT** configurations, they again become oscillatory with first neighbor being strongly ferromagnetic and second and third neighbors being slightly anti-ferromagnetic; the only exception being Mn_2NiSn where the second and third neighbor anti-ferromagnetic interactions are stronger than the first neighbor ferromagnetic one. The Ni-MnI interactions become weak and predominantly anti-ferromagnetic as one goes from **OC** to **DC** configurations where they are predominantly ferromagnetic. Under tetragonal distortions in the **DC** confi-

urations, the first neighbor interactions change to become slightly ferromagnetic offering no other significant changes. The MnII-MnII interactions vary qualitatively quite a bit across materials. In the **OC** configurations, they are oscillatory in case of Mn_2NiSn with dominant interactions being ferromagnetic. For the other two materials, the interactions are primarily ferromagnetic and weaker in comparison to Mn_2NiSn . The anti-site disorder keeps the interactions largely intact except that they are weaker in Mn_2NiSn . The tetragonal distortions modify these interactions significantly by making them more oscillatory. However, the strengths of the ferromagnetic and anti-ferromagnetic components in the oscillatory exchange interactions are nearly equal and thus compensate. To summarize, the magnetic exchange interactions in these materials are thus influenced by the inter-sublattice interactions and changes in their relative strengths upon changes in structures and configurations help make connections to the trends in the magnetic properties.

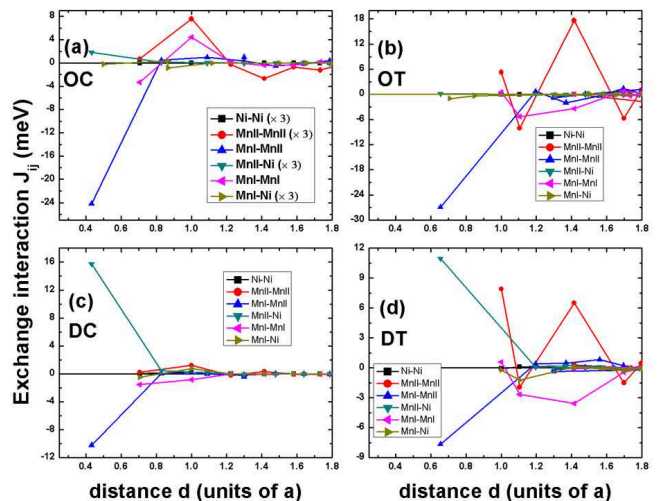


FIG. 7. (Color online) Magnetic exchange interactions (J_{ij}) as a function of inter-atomic distance d for Mn_2NiSn . Panel (a), (b), (c) and (d) represent ordered cubic (**OC**), ordered tetragonal (**OT**), disordered cubic (**DC**) and disordered tetragonal (**DT**) configurations, respectively.

IV. CONCLUSIONS

By means of *ab initio* calculations, we have investigated compositional and structural stabilities along with the magnetic properties of inverse Heusler Mn_2NiX alloys in connection to the improvement of shape memory and magneto-caloric effects. We find that the three out of four alloys considered here are potentially better shape memory materials as a large value of ΔM can be achieved even in these compositions whereas in prototype Ni_2MnX systems, one has to vary the ratio of Ni, Mn and X judiciously to achieve the same. We also find that these ma-

materials would show inverse magneto-caloric effect, which is technologically desirable for green environment. Our analysis reveal that these properties emerge due to the inverse Heusler structure where the two Mn atoms are inequivalent and an anti-site disorder exists between one of the Mn and the Ni sublattices. It is also found that the electronic structures associated with the Mn atom, which makes an alloy with Ni, are primarily responsible for the dramatic changes in the magnetic properties, and consequently for improved functionalities. This work, thus, show that the Mn_2NiX alloys in the inverse Heusler structure can be considered as potential functional materials and that more experimental verifications of their functional properties are required.

V. ACKNOWLEDGMENTS

Financial assistance from the Swedish Research Links (VR-SIDA) is acknowledged. The Swedish National Computing facilities, computation facilities from C-DAC, Pune, India and from Department of Physics, IIT Guwahati funded under the FIST programme of DST, India are also acknowledged.

- ¹F. X. Hu, B. G. Shen, and J. R. Sun, *Appl. Phys. Lett.* **76**, 3460 (2000).
- ²L. Pareti, M. Solzi, F. Albertini, and A. Paoluzi, *Eur. Phys. J. B* **32**, 303 (2003).
- ³T. Krenke, E. Duman, M. Acet, E. F. Wassermann, X. Moya, L. Mañosa, and A. Planes, *Nature Mater.* **4**, 450 (2005).
- ⁴A. Planes, L. Mañosa and M. Acet, *J. Phys. Condens. Matter.* **21**, 233201 (2009).
- ⁵L. Mañosa, D. González-Alonso, A. Planes, E. Bonnot, M. Barrio, J. Tamarit, S. Aksoy and M. Acet, *Nat Mater* **9** 478 (2010).
- ⁶P. O. Castillo-Villa, D. E. Soto-Parra, J. A. Matutes-Aquino, R. A. Ochoa-Gamboa, A. Planes, L. Mañosa, D. González-Alonso, M. Stipcich, R. Romero, D. Rios-Jara, and H. Flores-Zuñiga, *Phys. Rev. B* **83**, 174109 (2011).
- ⁷C. Biswas, R. Rawat, and S. R. Barmana, *Appl. Phys. Lett.* **86**, 202508 (2005).
- ⁸V. K. Sharma, M. K. Chattopadhyay, K. H. B. Shaeb, A. Chouhan and S. B. Roy, *Appl. Phys. Lett.* **89**, 222509 (2006).
- ⁹Z. Li, C. Jing, J. Chen, S. Yuan, S. Cao, and J. Zhang, *Appl. Phys. Lett.* **91**, 112505 (2007).
- ¹⁰V. K. Sharma, M. K. Chattopadhyay, and S. B. Roy, *Phys. Rev. B* **76**, 140401R (2007).
- ¹¹D. Y. Cong, S. Roth, J. Liu, Q. Luo, M. Potschke, C. Hurrich, and L. Schultz, *Appl. Phys. Lett.* **96**, 112504 (2010).
- ¹²Y. Wang, C. Huang, H. Wu, J. Gao, S. Yang, D. Wang, X. Ding, X. Song, and X. Ren, *Appl. Phys. Lett.* **102**, 141909 (2013).
- ¹³L. Ma, W. H. Wang, C. M. Zhen, D. L. Hou, X. D. Tang, E. K. Liu and G. H. Wu, *Phys. Rev. B* **84**, 224404 (2011).
- ¹⁴H. Luo, F. Meng, Z. Feng, Y. Li, W. Zhu, G. Wu, X. Zhu, C. Jiang and H. Xu, *J. Appl. Phys.* **107**, 013905 (2010).
- ¹⁵K. Ullakko, J. K. Huang, C. Kanter, R. C. O'Handley and V. V. Kokorin, *Appl. Phys. Lett.* **69**, 1966 (1996).
- ¹⁶A. Sozinov, A. A. Likhachev, N. Lanska and K. Ullakko, *Appl. Phys. Lett.* **80**, 1746 (2002).
- ¹⁷P. Entel, A. Banneberg, M. Siewert, H. C. Harper, M. E. Gruner, D. Comtesse, H. Elmers and M. Kallmayer, *Metall. Mater. Trans. A* **43**, 2891 (2012).
- ¹⁸P. Entel, M. Siewert, M. E. Gruner, A. Chakrabarti, S. R. Barman, V. V. Sokolovskiy and V. D. Buchelnikov, *J. Alloys Compd.*, **577**, S107 (2013).
- ¹⁹R. B. Helmholdt and K. H. J. Buschow, *J. Less-Common Met.* **128**, 167 (1987).
- ²⁰G. D. Liu, J. L. Chen, Z. H. Liu, X. F. Dai, G. H. Wu, B. Zhang, and X. X. Zhang, *Appl. Phys. Lett.* **87**, 262504 (2005).
- ²¹N. Lakshmi, K. Pandey and N. Venugopalan, *Bull. Mater. Sci.* **25**, 309 (2002).
- ²²S. Paul, and S. Ghosh, *J. Appl. Phys.* **110**, 063523 (2011).
- ²³P. J. Brown, T. Kanomata, K. Neumann, K. -U. Neumann, B. Ouladdiaf, A. Sheikh and K. R. A. Ziebeck, *J. Phys. Condens. Matter.* **22**, 506001 (2010).
- ²⁴S. Singh, R. Rawat, S. E. Muthu, S.W. D'Souza, E. Suard, A. Senyshyn, S. Banik, P. Rajput, S. Bhardwaj, A. M. Awasthi, Rajeev Ranjan, S. Arumugam, D. L. Schlögl, *Phys. Rev. Lett.* **109**, 246601 (2012).
- ²⁵S. W. D'Souza, A. Chakrabarti and S. R. Barman <http://arXiv.org/abs/1310.6130v1> (2013).
- ²⁶S. Paul, S. Ghosh and B. Sanyal, *J. Phys. Condens. Matter.* **25**, 236005 (2013).
- ²⁷H. Ebert, D. Ködderitzsch and J. Minar, *Rep. Prog. Phys.* **74**, 096501 (2011)
- ²⁸see <http://olymp.cup.uni-muenchen.de/ak/ebert/SPRKKR>. SPR-KKR is a high quality Density Functional Theory based electronic structure code, co-ordinated by H. Ebert.
- ²⁹S. H. Vosko, L. Wilk and M. Nusair, *Can. J. Phys.* **58**, 1200 (1980).
- ³⁰P. Soven, *Phys. Rev.* **156**, 809 (1967).
- ³¹I. Liechtenstein, M. I. Katsnelson, V. A. Antropov and V. P. Gubanov, *J. Magn. Magn. Mater.* **67**, 65 (1987).
- ³²M. Methfessel and J. Köubler, *J. Phys. F: Met. Phys.* **12**, 141 (1982).
- ³³G. Grimvall, *Phys. Scr.* **13**, 59 (1976)
- ³⁴P. Söderlind and B. Johansson, *Thermochim. Acta* **218**, 145 (1993)
- ³⁵G. Kresse and J. Furthmüller, *Phys. Rev.* **B54**, 11169 (1996)
- ³⁶G. Kresse and D. Joubart, *Phys. Rev.* **B59**, 1758 (1999)
- ³⁷A. Zunger, S.-H. Wei, L. Ferreira, and J. E. Bernard, *Phys. Rev. Lett.* **65**, 353 (1990)
- ³⁸A. Van de Walle, P. Tiwary, M. de Jong, D.L. Olmsted, M. Asta, A. Dick, D. Shin, Y. Wang, L.-Q. Chen and Z.-K. Liu, *CAL-PHAD*, **42**, 13 (2013)
- ³⁹V. V. Godlevsky and K. M. Rabe, *Phys. Rev.* **B63**, 134407 (2001).